LARGE KERNEL NETWORK FOR IMAGE RESTORATION

Anonymous authors

000

001 002 003

004

006

008 009

010

011

012

013

014

016

017

018

019

021

024

025

026

027 028

029

031

033

034

037

040

041

042

043

044

046

047

048

051

052

Paper under double-blind review

ABSTRACT

The pursuit of large receptive fields has shaped the evolution of computer vision frameworks, spanning from convolutional neural networks (CNNs) to Transformers and Mamba. Recently, large-kernel operations have revitalized CNNs, making them competitive once again and widely applicable across diverse vision tasks. However, scaling kernel sizes inevitably results in substantial growth in both parameters and computational overhead. Consequently, existing approaches are often limited to small kernels or resort to decoupled designs for large kernels. In this paper, we propose a simple and efficient large kernel network for image restoration, termed ArtIR, motivated by the channel redundancy observed in image restoration models. Specifically, ArtIR applies adaptive large-kernel operations to a collapsed single channel and employs an ultra-lightweight channel attention mechanism to restore channel diversity. To complement local features, we further introduce a large kernel fusion module that integrates multi-scale information. Unlike most prior methods that focus on a narrow set of restoration tasks, we comprehensively evaluate ArtIR across single-degradation, all-in-one, and composite degradation scenarios. Beyond generic restoration, we also assess our model on domain-specific applications such as ultra-high-definition restoration, medical imaging, and remote sensing. Extensive experiments demonstrate that ArtIR achieves state-of-the-art performance while maintaining high efficiency and fast inference.

1 Introduction

Image restoration aims to reconstruct a high-quality image from a low-quality observation. Expanding the receptive field is essential for modeling robust long-range pixel dependencies, which has long been regarded as one of the central challenges in this field. Early approaches sought to enlarge the receptive fields of CNNs through techniques such as dilated convolutions and the use of deeper network architectures. Recently, Transformer and Mamba architectures have been introduced to this domain, owing to their strong capacity for capturing long-range dependencies (Ali et al., 2023).

More recently, large-kernel CNNs have reemerged, showing impressive performance in high-level vision tasks (Chen et al., 2024a; Li et al., 2025b; Liu et al., 2022; 2023; Ding et al., 2022a; Yasuki & Taki, 2024; Wang & Xi, 2025; Li et al., 2025d; Liu et al., 2025; Li et al., 2023b). These advances are largely motivated by insights into the success of Transformers, particularly the role of self-attention mechanisms in enabling large receptive fields. Leveraging large kernel sizes, CNN-based approaches have matched or even surpassed state-of-the-art Transformers. As a result, efficiently expanding receptive fields in CNNs has become one of the central themes in computer vision.

This trend has also extended to the field of image restoration. A widely adopted strategy is to decouple large-kernel convolutions into more computationally efficient components (Wang et al., 2024c; Luo et al., 2023; Ruan et al., 2023), such as smaller depth-wise convolutions, depth-wise dilated convolutions, and point-wise convolutions. For example, LKD (Luo et al., 2023) demonstrates that a 13×13 depth-wise convolution can be decomposed into a 5×5 depth-wise convolution and a 5×5 depth-wise dilated convolution with a dilation rate of 3. However, such decompositions fail to provide direct interactions among pixels within large windows, thereby reducing the representational capacity of the model. To address this limitation, several works apply unabridged large-kernel convolutions directly to feature maps (Hu et al., 2025b; Lee et al., 2024). For instance, OKNet (Cui et al., 2024b) employs a 63×63 depth-wise convolution to capture large-scale contextual information. Although placed in the bottleneck, its full-channel operation still introduces substantial computational overhead. Processing a 4K (i.e., 3840×2160) image, for example, requires approximately 4 GFLOPs

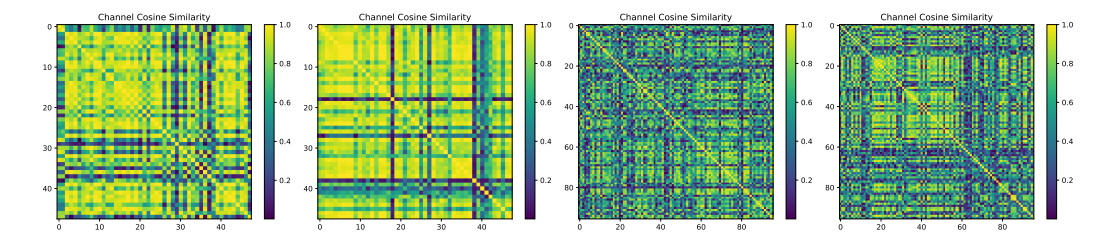


Figure 1: Visualization of channel-wise cosine similarity in Restormer (Zamir et al., 2022), where brighter colors indicate higher similarity. Additional examples are provided in the Appendix.

for each additional feature channel in the bottleneck. Another popular line of research employs frequency-domain processing to modulate global information (Zhou et al., 2023; Cui et al., 2024b; Mao et al., 2023; Li et al., 2023a). The typical pipeline involves transforming spatial features into the spectral domain, applying convolutions for modulation, and then converting the modulated spectra back to the spatial domain. However, frequency-based approaches struggle to explicitly model relationships between specific pixels. Moreover, they often introduce significant computational complexity, particularly when applied to high-resolution feature maps (Li et al., 2023a).

To address the aforementioned limitations, we propose a novel approach that leverages large-kernel operations to construct an efficient image restoration network. Our method is motivated by the observation of channel redundancy in image restoration models. As illustrated in Figure 1, we visualize the cosine similarity among channels at different scales in a representative baseline, Restormer (Zamir et al., 2022). The results reveal substantial redundancy across channels, with additional visualizations for other models provided in the Appendix. Guided by this observation, our design applies large-kernel operations to a collapsed single channel. To restore channel diversity, we introduce a lightweight channel attention mechanism that modulates feature channels, thereby striking a balance between efficiency and information preservation. This strategy enables the use of extremely large kernels while avoiding the computational burden of applying them to all channels.

Nevertheless, relying solely on large-kernel operations may lead to feature oversmoothing. To address this, we introduce a large kernel fusion module that enables interactions between local—large and large—large receptive fields, thereby enhancing multi-scale representation learning. The module partitions channels into two groups: one progressively enlarges receptive fields, while the other focuses on embedding local signals. Importantly, this design is also partly motivated by channel redundancy. Rather than relying on convolutional layers, the module matches the channel counts between groups by replicating features, which effectively reduces both parameter count and computational overhead.

On the other hand, most existing restoration models are evaluated on a narrow set of tasks, typically focusing on a single setting. To more comprehensively demonstrate the effectiveness of ArtIR, we conduct evaluations across multiple mainstream scenarios, including single-degradation, all-in-one, and composite degradation settings¹. In addition, since image restoration has extensive applications in specialized domains, we further evaluate our method on domain-specific tasks, including ultra-high-definition (UHD), medical imaging, and remote sensing. The main contributions are as follows:

- We propose a novel solution for leveraging large-kernel operations, inspired by the channel characteristics observed in restoration models. Specifically, our design applies large-kernel operations to a collapsed single channel, complemented by lightweight channel attention to recover channel diversity, thereby achieving a better trade-off between efficiency and information preservation.
- We introduce a large kernel fusion module that enhances multi-scale representation learning by enabling interactions between local-local and local-large receptive fields.
- We conduct comprehensive experiments on both generic tasks (single-degradation, all-in-one, and composite degradation) and domain-specific tasks (UHD, medical imaging, and remote sensing). The results show that the proposed model, ArtIR, achieves state-of-the-art performance while preserving high efficiency and fast inference speed (see Figure 2 and Table 13).

¹In the single-degradation setting, the model is trained separately for specific tasks such as dehazing and desnowing. In the all-in-one setting, the model is trained on a compound dataset that integrates multiple tasks, where each image is degraded by only one type of distortion. After training, the model can address all these tasks. In the composite degradation setting, each image contains multiple degradation types simultaneously.

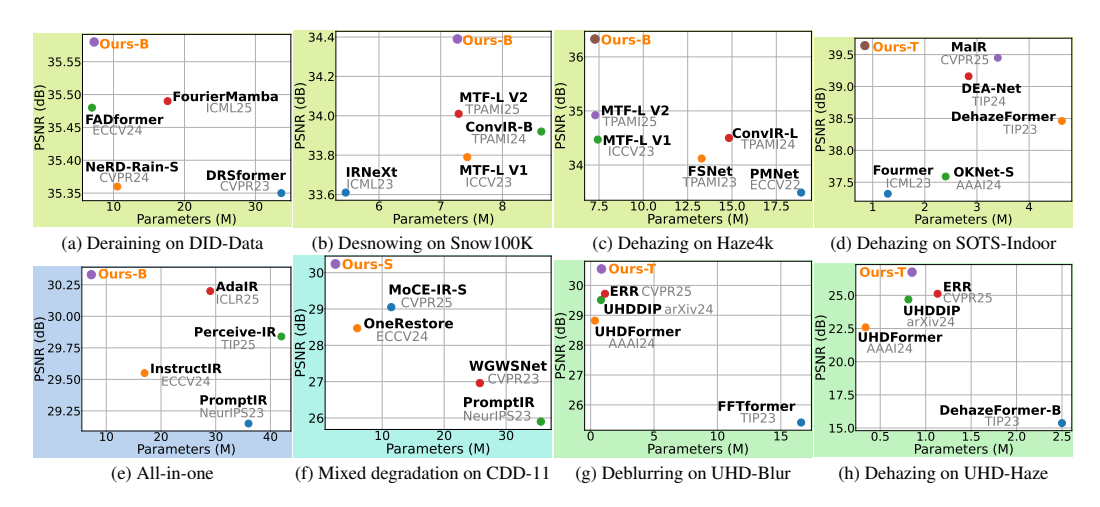


Figure 2: Comparison of parameter efficiency and PSNR under various image restoration scenarios: single-degradation, all-in-one, composite degradation, and ultra-high-definition.

2 RELATED WORK

Image restoration. Recent deep learning frameworks have substantially advanced image restoration and can be broadly categorized into CNN-based, Transformer-based, and Mamba-based approaches. A key driving factor behind these architectures is the pursuit of large-kernel operations, which enable robust large-scale receptive fields and thereby improve the removal of severe degradations.

To overcome the local connectivity limitation of convolution operators, CNN-based methods typically enlarge receptive fields by stacking deeper layers, employing strip operations, applying dilated convolutions, or adopting multi-stage paradigms (Zhang et al., 2018b; Ren et al., 2016; 2020; Cui et al., 2023c; Son et al., 2021; Hao et al., 2024). Subsequently, Transformer-based models, empowered by self-attention, have further improved performance across diverse restoration tasks such as dehazing, deraining, and deblurring (Guo et al., 2022; Chen et al., 2023; Song et al., 2023; Qiu et al., 2023; Jin et al., 2025; Tsai et al., 2022; Zamir et al., 2022; Wang et al., 2022; Kong et al., 2023; Liang et al., 2021; Chen et al., 2021a). However, this success comes at the cost of the quadratic complexity of self-attention with respect to input size. Although several strategies restrict the attention region or alter the computation dimension, obtaining large-scale receptive fields with high efficiency remains challenging. More recently, Mamba-based frameworks have been introduced to implicitly capture long-range dependencies by propagating contextual information through advanced scanning strategies (Li et al., 2025a; Guo et al., 2024a; Luan et al., 2025; Weng et al., 2024; Li et al., 2025c; Zou et al., 2024). In contrast to these approaches, we propose a new solution that leverages large-kernel operations to achieve efficient, effective, and explicit modeling of long-range pixel correlations.

Large kernel network. The success of Transformers has been attributed to several factors, including their advanced architecture (Yu et al., 2022), frequency bias (Park & Kim, 2022), and capacity to capture long-range dependencies (Vaswani et al., 2017). More recently, increasing attention has been directed toward their ability to model large receptive fields. Following this trend, CNNs have reemerged in high-level vision tasks by incorporating large kernels (Liu et al., 2022; 2023; Ding et al., 2022a; Chen et al., 2024a; Ding et al., 2022b; Xu et al., 2023; Li et al., 2025b; Ding et al., 2024).

Inspired by this development (Xie et al., 2023; Wang et al., 2024c), several image restoration methods adopt kernel decomposition, factorizing a large-kernel convolution into smaller components (Wang et al., 2024c; Ruan et al., 2023; Luo et al., 2023), such as depth-wise and dilated convolutions. However, such decomposition inevitably reduces representational capacity. Other approaches directly apply intact large-kernel convolutions in square or stripe form (Cui et al., 2024b; Hu et al., 2025b; Lee et al., 2024; 2025; Shi et al., 2024), but applying these operations across many channels leads to substantial computational overhead. An alternative direction leverages frequency-domain processing, such as the Fourier transform, to encode global information according to the convolution theorem (Zhou et al., 2023; Mao et al., 2023; Cui et al., 2023a; Li et al., 2023a). Yet, this strategy struggles to explicitly model pixel-wise relationships and introduces additional complexity due to reliance on transformer-based tools (Li et al., 2023a).

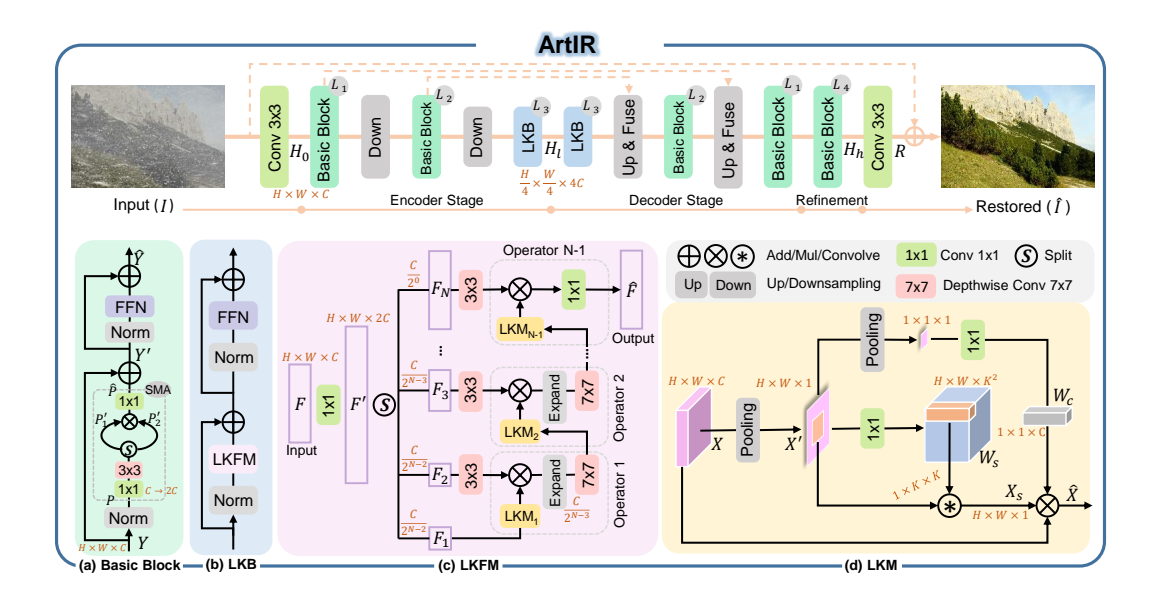


Figure 3: **Architecture of ArtIR.** The network follows a U-shaped learning paradigm and is primarily composed of (a) the Transformer-style basic block and (b) the large-kernel block (LKB). The (c) large-kernel fusion module (LKFM) enables multi-scale learning by progressively integrating large-scale contextual information of different sizes with local details. The (d) large-kernel module (LKM) applies large-kernel operations to a single-channel feature map, complemented by a lightweight channel attention mechanism to enhance channel diversity, thereby balancing efficiency and information preservation. The *Expand* operation doubles the channel dimension via duplication.

3 METHODOLOGY

This section presents the design of ArtIR for image restoration, including the pipeline and its two core components, the Large Kernel Module (LKM) and the Large Kernel Fusion Module (LKFM).

Overall pipeline. The pipeline of ArtIR is illustrated in the top part of Figure 3. ArtIR adopts a U-shaped Transformer-style architecture, consisting of an encoder, a decoder, and a refinement stage (Zamir et al., 2022). Both the encoder and decoder comprise multiple Basic Blocks, while the Large Kernel Block (LKB) is applied only in the bottleneck to reduce computational overhead (Cui et al., 2024b). Given a degraded image $I \in \mathbb{R}^{H \times W \times 3}$, ArtIR first employs a 3×3 convolution to extract shallow features $H_0 \in \mathbb{R}^{H \times W \times C}$. These features are then processed by a three-scale encoder to produce low-resolution representations $H_l \in \mathbb{R}^{\frac{H}{4} \times \frac{W}{4} \times 4C}$. The decoder takes H_l as input and progressively reconstructs high-resolution features. During this process, encoder and decoder features are concatenated through residual connections and fused by a 1×1 convolution. Finally, a refinement stage (Zamir et al., 2022) further enhances the features, yielding $H_h \in \mathbb{R}^{H \times W \times C}$. The restored residual image $R \in \mathbb{R}^{H \times W \times 3}$ is then generated using a 3×3 convolution, and the final restored output is obtained by $\hat{I} = R + I$.

The architecture of the basic block is illustrated in Figure 3(a). The basic block follows a Transformer-style design and incorporates a gated mechanism, termed self-modulated attention (SMA), to control information flow, inspired by its success in computer vision (Zamir et al., 2022; Ma et al., 2024a;b). Formally, given input features $Y \in \mathbb{R}^{H \times W \times C}$, the computation in a basic block is expressed as

$$\hat{Y} = \text{FFN}(\text{Norm}(Y')) + Y', \text{ where } Y' = \text{SMA}(\text{Norm}(Y)) + Y,$$
 (1)

where Norm, FFN, and SMA denote layer normalization, the feed-forward network, and self-modulated attention, respectively. For simplicity, we adopt the FFN design from Restormer (Zamir et al., 2022). Given input features $P \in \mathbb{R}^{H \times W \times C}$, the SMA is further defined as

$$\hat{P} = \operatorname{Conv}_{1 \times 1}(P_1' \otimes P_2'), \quad \text{where} \quad P_1', P_2' = \operatorname{Split}(\operatorname{Conv}_{3 \times 3}^{\operatorname{DW}}(\operatorname{Conv}_{1 \times 1}(P))) \in \mathbb{R}^{H \times W \times C}, \quad (2)$$

where $\operatorname{Conv}_{1\times 1}$ and $\operatorname{Conv}_{3\times 3}^{\operatorname{DW}}$ denote a 1×1 convolution and a 3×3 depthwise convolution, respectively; Split indicates channel-wise feature partitioning, and \otimes represents element-wise multiplication.

Figure 3(b) illustrates the LKB, which largely follows the structure of the basic block, except that the SMA is replaced with the LKFM. We next describe the LKFM and its core component, the LKM.

3.1 LARGE KERNEL MODULE (LKM)

Motivation. Existing large-kernel operations are mainly implemented through kernel decoupling, direct application, or frequency-domain processing. However, as the number of channels increases, particularly in the bottleneck, the computational overhead of such operations grows substantially. Figure 1 shows that channels exhibit strong similarity, indicating that only a subset may need to be modulated without compromising performance. Motivated by this, we apply large-kernel operations to a collapsed single channel and design a lightweight channel attention mechanism to restore channel diversity. This design provides a new perspective on balancing efficiency and representation power.

Architecture. As shown in Figure 3(d), given input features $X \in \mathbb{R}^{H \times W \times C}$, we first apply average pooling to obtain a collapsed single channel $X' \in \mathbb{R}^{H \times W \times 1}$, which is then processed by large-kernel operations. To enhance adaptability across different datasets and tasks, the large-kernel operation is implemented as a learnable convolution with pixel-wise adaptive parameters, formally defined as

$$X_s = W_s \circledast X', \text{ where}$$
 (3)

$$W_s = \operatorname{Conv}_{1 \times 1}(X') \in \mathbb{R}^{H \times W \times K^2},$$
 (4)

where W_s denotes the learnable parameters of the $K \times K$ large-kernel convolution, and X_s is the spatially modulated single-channel feature map. The symbol (*) denotes convolution. To determine K, we conduct preliminary experiments with kernel sizes ranging from 3 to 63, with implementation details provided in the Appendix. Figure 4 shows that performance consistently improves with larger kernels. Remarkably, this increase in kernel size introduces only 0.02M additional parameters and 0.06G FLOPs. Based on these results, we set K=63.

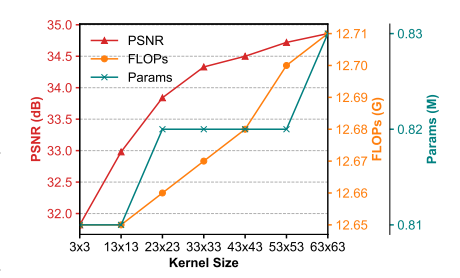


Figure 4: Experimental results with kernel sizes ranging from 3 to 63.

As large-kernel learning is performed only on a single channel, we introduce a lightweight channel attention to restore channel diversity. Specifically, average pooling is used to X' to obtain single-channel global information, which is then passed through a 1×1 convolution to generate channel-wise attention weights $W_c\in\mathbb{R}^{1\times 1\times C}$. These weights are applied to the input X for channel modulation. Compared with regular full-size attention (Chen et al., 2022), which learns channel weights directly from the input of size $H\times W\times C$, our lightweight design significantly reduces parameter count while preserving performance. Finally, the output of the LKM is given by $\hat{X}=\mathrm{LKM}(X)=X_s\otimes X\otimes W_c$.

3.2 Large Kernel Fusion Module (LKFM)

Our LKM effectively captures explicit long-range dependencies through large-kernel operations; however, it may overlook local and multi-scale information, which is critical for handling degradations of varying sizes in image restoration. To address this limitation, we propose the LKFM, which facilitates interactions between local—large and large—large receptive fields. Specifically, the input features are divided into two groups along the channel dimension: one group progressively enlarges the receptive field up to 63×63 , while the other continually embeds local information into the first group. We employ an octave-like channel partition and kernel-scaling strategy to allocate larger kernels to more channels. Moreover, inspired by channel redundancy, we match the channel counts between groups through simple feature replication, thereby further improving efficiency.

Formally, given input features $F \in \mathbb{R}^{H \times W \times C}$, LKFM first expands the channel dimension using a 1×1 convolution, producing $F' \in \mathbb{R}^{H \times W \times 2C}$ for subsequent operations. F' is then partitioned into N channel segments, $\{F_1, \ldots, F_N\}$, which are further grouped into $F_1 \in \mathbb{R}^{H \times W \times \frac{C}{2^N - 2}}$ and $\{F_2, \ldots, F_n, \ldots, F_N\}$ with $F_n \in \mathbb{R}^{H \times W \times \frac{C}{2^N - n}}$. The segment F_1 is recursively processed by a sequence of operators (see Figure 3(c)), primarily involving LKM with a specific kernel size K. For the i^{th} operator ($i \in [1, N-2]$), the computation is formally defined as

$$\hat{F}_i = \operatorname{Conv}_{7\times7}^{\operatorname{DW}}(\operatorname{Expand}(\tilde{F}_i)), \text{ where } \tilde{F}_i = \operatorname{LKM}_i(Z) \otimes \operatorname{Conv}_{3\times3}^{\operatorname{DW}}(F_{i+1}),$$
 (5)

270 271 272

279

281

284

287

288

289

290

291

292

293

295

296 297

298

299

300

301

302

303

304

305 306

307 308

310

311

312

313

314

315

316

317

318

319 320

321

322

323

Table 1: Desnowing results on Snow100K and CSD.

Tuble 1. Desilowing	, resu	165 01	1 5110	** 100	IX unc	1 000
Method		100K SSIM	CS PSNR		Params (M)	FLOPs (G)
IRNeXt (Cui et al., 2023c) MTF-L V1 (Qiu et al., 2023) ConvIR-B (Cui et al., 2024a) MTF-L V2 (Jin et al., 2025)	33.79 33.92	0.95 0.96		-	5.46 7.43 8.63 7.29	42.1 88.1 71.2 86.0
Ours-B	34.39	0.96	39.43	0.99	7.27	63.14

Table 2: Dehazing results on Haze4k.

Method	PSNR	SSIM	Params	FLOPs
PMNet (Ye et al., 2022)	33.49	0.98	18.90	81.1
FSNet (Cui et al., 2023b)	34.12	0.99	13.29	110.5
MTF-L V1 (Qiu et al., 2023)	34.47	0.99	7.43	88.1
ConvIR-L (Cui et al., 2024a)	34.50	0.99	14.83	129.9
MTF-L V2 (Jin et al., 2025)	34.92	0.99	7.29	86.0
Ours-B	36.33	0.99	7.27	63.14

Table 3: Dehazing results on SOTS-Indoor.

Table 4: Deraining results on DID and SPA

Method	PSNR SSIM	Params	FLOPs			-Data		-Data	
DeHamer (Guo et al., 2022)	36.63 0.988	132.45	48.93	Method	PSNR	SSIM	PSNR	SSIM	Params
Fourmer (Zhou et al., 2023)	37.32 0.990	1.29	20.6	Restormer (Zamir et al., 2022)	35.29	0.9641	47.98	0.9921	26.13
DehazeFormer (Song et al., 2023)	38.46 0.994	4.63	48.64	DRSformer (Chen et al., 2023)	35.35	0.9646	48.54	0.9924	33.65
OKNet-S (Cui et al., 2024b)	37.59 0.994	2.40	17.86	NeRD-Rain-S (Chen et al., 2024b)	35.36	0.9647	48.90	0.9936	10.53
DEA-Net (Chen et al., 2024c)	39.16 0.992	2.84	24.88	FADformer (Gao et al., 2024)	35.48	0.9657	49.21	0.9934	6.96
MaIR (Li et al., 2025a)	39.45 0.997	3.40	24.03	FourierMamba (Li et al., 2025c)	35.49	0.9659	49.18	0.9931	17.62
Ours-T	39.64 0.997	0.85	12.76	Ours-B	35.58	0.9664	49.54	0.9939	7.27

where \hat{F}_i represents the output and Z the input feature, which can be either F_1 (i=1) or \hat{F}_{i-1} . The Expand operation adjusts channel dimensions across scales by duplicating features twice along the channel dimension, motivated by observations of channel redundancy. A 7×7 depthwise convolution is then applied to refine the coarsely expanded features. Compared with convolution-based expansion, this strategy substantially reduces parameters while achieving comparable performance. The final operator employs a 1×1 convolution to generate the output of the LKFM. In our implementation, the last operator uses a kernel size of 63, while preceding operators adopt progressively smaller kernels in an octave-like manner, i.e., $\left| \frac{63}{2^{N-1-i}} \right|$. Notably, the LKFM introduces only negligible computational overhead compared to its single-scale counterpart, yet yields significant performance gains.

EXPERIMENTAL RESULTS

To evaluate the effectiveness of the proposed ArtIR, we conduct extensive experiments on three representative image restoration tasks: (a) single-degradation, (b) all-in-one, and (c) composite degradation. We further extend the evaluation to domain-specific tasks, including (d) UHD (3840×2160), (e) medical imaging, and (f) remote sensing. In the result tables, the best and second-best performances are highlighted in magenta and blue, respectively. To balance performance and efficiency, we scale our model by adjusting the number of blocks and channels across stages, yielding three variants. Additional details on the datasets and training configurations are provided in the Appendix.

4.1 SINGLE-DEGRADATION IMAGE RESTORATION RESULTS

In this setting, ArtIR is evaluated on six synthetic and real-world datasets spanning three image restoration tasks: desnowing, dehazing, and deraining. Separate models are trained for each dataset.

Image desnowing. We evaluate ArtIR on two widely used desnowing datasets: Snow100K (Liu et al., 2018) and CSD (Chen et al., 2021b). Table 1 shows that our approach significantly outperforms recent competitive methods. Notably, it achieves a 0.38 dB PSNR improvement over the Transformer-based MTF-L V2 (Jin et al., 2025), while using similar parameters and incurring lower computational cost.

Image dehazing. We evaluate dehazing performance on Haze4K (Liu et al., 2021), with results reported in Table 2. Our model achieves a substantial improvement over MTF-L V2 (Jin et al., 2025). We further compare against lightweight dehazing models on SOTS-Indoor (Li et al., 2018). Table 3 shows that our tiny variant surpasses the Mamba-based MaIR (Li et al., 2025a) by 0.19 dB in PSNR, while reducing parameters by 75% and FLOPs by 47%, highlighting the efficiency of our design.

Image deraining. We compare our model with state-of-the-art deraining algorithms on the synthetic DID-Data (Zhang & Patel, 2018) and real-world SPA-Data (Wang et al., 2019) datasets. As shown in Table 4, our model performs strongly in both synthetic and real-world scenarios. On the real-world dataset in particular, it achieves substantial gains over the frequency-based FourierMamba (Li et al., 2025c) in both PSNR and SSIM, while requiring only 41% of the parameters.

Table 5: Quantitative comparisons under the all-in-one image restoration setting.

		Dehazing SOTS		Deraining Rain100L		Denoising BSD68		Deblurring GoPro		Low-Light LOLv1		Average	
Method	Params	PSNR	SSIM	PSNR	SSIM	PSNR	SSIM	PSNR	SSIM	PSNR	SSIM	PSNR	SSIM
Restormer (Zamir et al., 2022)	26M	24.09	0.927	34.81	0.962	31.49	0.884	27.22	0.829	20.41	0.806	27.60	0.881
TransWeather (Valanarasu et al., 2022)	38M	21.32	0.885	29.43	0.905	29.00	0.841	25.12	0.757	21.21	0.792	25.22	0.836
IDR (Zhang et al., 2023)	15M	25.24	0.943	35.63	0.965	31.60	0.887	27.87	0.846	21.34	0.826	28.34	0.893
PromptIR (Potlapalli et al., 2023)	36M	26.54	0.949	36.37	0.970	31.47	0.886	28.71	0.881	22.68	0.832	29.15	0.904
InstructIR-5D (Conde et al., 2024)	17M	27.10	0.956	36.84	0.973	31.40	0.873	29.40	0.886	23.00	0.836	29.55	0.908
Perceive-IR (Zhang et al., 2025a)	42M	28.19	0.964	37.25	0.977	31.44	0.887	29.46	0.886	22.88	0.833	29.84	0.909
AdaIR (Cui et al., 2025)	29M	30.53	0.978	38.02	0.981	31.35	0.889	28.12	0.858	23.00	0.845	30.20	0.910
Ours-B	7M	30.62	0.978	38.08	0.983	31.47	0.893	29.38	0.884	22.12	0.855	30.33	0.919

Table 6: PSNR scores of directly applying the pre-trained all-in-one model to three denoising datasets: BSD68 (Martin et al., 2001), Urban100 (Huang et al., 2015) and Kodak24 (Rich, 1999).

		BSD68			Urban100)		Kodak24		
Method	$\sigma=15$	$\sigma=25$	$\sigma = 50$	$\sigma=15$	$\sigma = 25$	$\sigma = 50$	$\sigma=15$	$\sigma = 25$	$\sigma = 50$	Average
TransWeather (Valanarasu et al., 2022)	31.16	29.00	26.08	29.64	27.97	26.08	31.67	29.64	26.74	28.66
IDR (Zhang et al., 2023)	34.11	31.60	28.14	33.82	31.29	28.07	34.78	32.42	29.13	31.48
InstructIR-5D (Conde et al., 2024)	34.00	31.40	28.15	33.77	31.40	28.13	34.70	32.26	29.16	31.44
AdaIR (Cui et al., 2025)	34.01	31.35	28.06	34.10	31.68	28.29	34.89	32.38	29.21	31.55
Ours-B	34.14	31.47	28.19	34.38	32.01	28.71	35.08	32.59	29.43	31.78

Table 7: Quantitative results on CDD-11 (Guo et al., 2024b) for composite degradation image restoration, which comprises 11 degradation categories. Results are reported in PSNR and SSIM.

Method	Params	Low	(L)	Haze	(H)	Rain	(R)	Snow	(S)	L+	Н	L+	R	L+	S	H+	R	H+	·S	L+H	I+R	L+H	I+S	Aver	age
			_	_	_	_	_	_	_	_	_	_	_	_	_	_	_	_	_	_	_	_	_	_	
AirNet	8.93M	24.83	.778	24.21	.951	26.55	.891	26.79	.919	23.23	.779	22.82	.710	23.29	.723	22.21	.868	23.29	.901	21.80	.708	22.24	.725	23.75	.814
PromptIR	35.6M	26.32	.805	26.10	.969	31.56	.946	31.53	.960	24.49	.789	25.05	.771	24.51	.761	24.54	.924	23.70	.925	23.74	.752	23.33	.747	25.90	.850
WGWSNet	25.76M	24.39	.774	27.90	.982	33.15	.964	34.43	.973	24.27	.800	25.06	.772	24.60	.765	27.23	.955	27.65	.960	23.90	.772	23.97	.771	26.96	.863
WeatherDiff	82.96M	23.58	.763	21.99	.904	24.85	.885	24.80	.888	21.83	.756	22.69	.730	22.12	.707	21.25	.868	21.99	.868	21.23	.716	21.04	.698	22.49	.799
OneRestore	5.98M	26.48	.826	32.52	.990	33.40	.964	34.31	.973	25.79	.822	25.58	.799	25.19	.789	29.99	.957	30.21	.964	24.78	.788	24.90	.791	28.47	.878
MoCE-IR-S	11.47M	27.26	.824	32.66	.990	34.31	.970	35.91	.980	26.24	.817	26.25	.800	26.04	.793	29.93	.964	30.19	.970	25.41	.789	25.39	.790	29.05	.881
Ours-S	2.46M	27.45	.837	35.93	.994	34.97	.974	36.99	.981	26.79	.836	26.78	.817	26.54	.809	32.10	.973	32.93	.976	26.00	.810	26.13	.809	30.24	.892

4.2 All-in-one image restoration results

Following prior works (Cui et al., 2025; Zhang et al., 2025a; Conde et al., 2024), the model is trained on a mixed dataset comprising five tasks and subsequently evaluated on each task. As shown in Table 5, our approach outperforms competing methods on most metrics, achieving average gains of 0.13 dB PSNR and 0.009 SSIM over the frequency-based AdaIR (Cui et al., 2025) across all datasets. Notably, this advantage is obtained with 76% fewer parameters and without reliance on explicit degradation priors, underscoring the strong representational capacity of our large-kernel design.

To further assess generalization, we apply the pre-trained all-in-one model to two additional denoising benchmarks, Urban100 (Huang et al., 2015) and Kodak24 (Rich, 1999). Table 6 demonstrates that the proposed model exhibits stronger robustness, surpassing the second-best method, AdaIR (Cui et al., 2025), on both datasets under different noise levels.

4.3 Composite degradation image restoration results

We further evaluate our model on CDD-11 (Guo et al., 2024b), a composite degradation benchmark where each image is affected by up to three degradation types. Results across all 11 categories are reported in Table 7. Our model achieves the best performance in every category and, on average, surpasses the recent dynamic MoCE-IR-S (Zamfir et al., 2025) by 1.19 dB in PSNR and 0.011 in SSIM. Notably, on the haze subset, the improvement reaches 3.27 dB in PSNR. Moreover, our model contains only 2.46M parameters, substantially fewer than prior methods. Figure 5 provides visual comparisons with leading approaches, illustrating the superior capability of our model in removing composite degradations from challenging examples.

4.4 Domain-specific image restoration results

To verify the generality of our design, we evaluate ArtIR on domain-specific tasks, including ultrahigh-definition (UHD), medical imaging, and remote sensing.

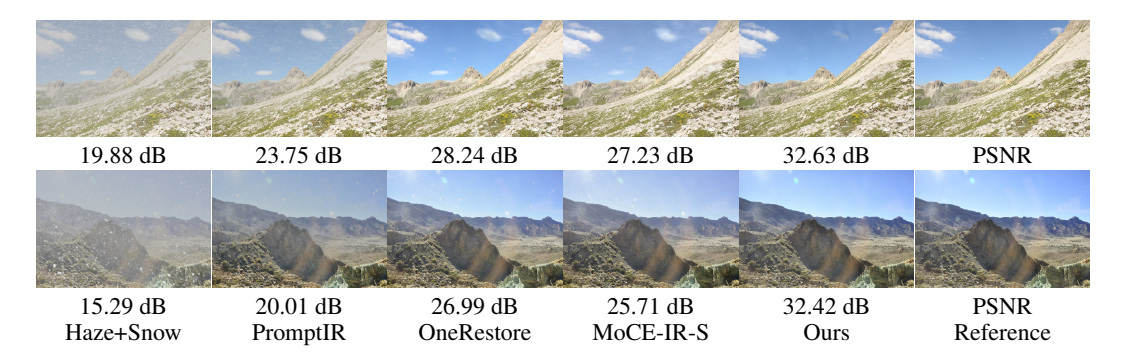


Figure 5: Visual results on CDD-11 (Guo et al., 2024b) for composite degradation image restoration.

Table 8: Dehazing results on UHD-Haze.

Table 9: Deblurring results on UHD-Blur.

Method	PSNR	SSIM	Params	Method	PSNR	SSIM	Params			
Zheng et al. (Zheng et al., 2021)	18.04	0.811	34.5M	Restormer (Zamir et al., 2022)	25.21	0.693	26.1M			
Restormer (Zamir et al., 2022)	12.72	0.693	26.1M	Uformer (Wang et al., 2022)	25.27	0.737	20.6M			
Uformer (Wang et al., 2022)	19.83	0.737	20.6M	Stripformer (Tsai et al., 2022)	25.05	0.725	19.7M			
DehazeFormer-B (Song et al., 2023)	15.37	0.725	2.5M	FFTformer (Kong et al., 2023)	25.41	0.725	16.6M			
UHDFormer (Wang et al., 2024a)	22.59	0.943	0.339M	UHDFormer (Wang et al., 2024a)	28.82	0.844	0.339M			
UHDDIP (Wang et al., 2024b)	24.69	0.952	0.81M	UHDDIP (Wang et al., 2024b)	29.51	0.858	0.81M			
ERR (Zhao et al., 2025)	25.12	0.950	1.131M	ERR (Zhao et al., 2025)	29.72	0.861	1.131M			
Ours-T	26.75	0.963	0.85M	Ours-T	30.55	0.877	0.85M			

AAPM (McCollough et al., 2017) dataset.

Table 10: CT image denoising results on the Table 11: PET image synthesis results on the PolarStar M660 (Yang et al., 2025) dataset.

Method	PSNR↑	SSIM↑	RMSE↓	Params	Method	PSNR↑	SSIM↑	RMSE↓	Params
TransCT (Zhang et al., 2021)	32.62	0.908	9.533	13.23	CycleWGAN (Zhou et al., 2020)	36.62	0.929	0.091	1.00
Eformer (Luthra et al., 2021)	33.35	0.918	8.803	0.34	DCITN (Zhou et al., 2022b)	36.09	0.929	0.097	0.08
CTformer (Wang et al., 2023)	33.25	0.913	8.897	1.45	DRMC (Yang et al., 2023)	36.00	0.935	0.100	0.62
DenoMamba (Öztürk et al., 2024)	33.53	0.915	8.612	112.62	ARGAN (Luo et al., 2022)	36.73	0.941	0.090	31.14
Restore-light (Yang et al., 2025)	33.64	0.918	8.514	1.16	Restore-light (Yang et al., 2025)	36.96	0.943	0.089	1.16
Ours-T	33.76	0.919	8.400	0.85	Ours-T	37.25	0.947	0.086	0.85

Table 12: Remote sensing image dehazing results on SateHaze1k. Table 13: Runtime efficiency.

							rable 13. Ramanic emercincy
Method	T/ PSNR	iin SSIM		erate	Th PSNR	ick	Task/Data Method Time/s Speedup
Method	PSNK	SSIM	PSINK	SSHVI	PSINK	SSIM	Desnowing MTF-L V2 1.01
AIDTransformer (Kulkarni & Murala, 2023)	21.09	0.884	23.56	0.929	19.18	0.804	Snow100K Ours-B 0.12 ×8.4
DehazeFormer (Song et al., 2023)	24.26	0.909	25.69	0.938	22.26	0.835	Dehazing MTF-L V2 0.83
EMPF (Wen et al., 2023)	22.69	0.896	25.17	0.932		0.822	Haze4k Ours-B 0.11 ×7.5
Trinity (Chi et al., 2023)	22.65	0.896	24.73	0.934	20.57	0.824	Mixed MoCE-IR-S 0.49
FocalNet (Cui et al., 2023a)	24.16	0.916	25.99	0.947	21.69	0.847	CDD-11 Ours-S 0.20 ×2.5
FMambaIR (Luan et al., 2025)	24.58	0.912	25.83	0.939	22.65	0.850	All-in-one AdaIR 0.16
Ours-S	25.18	0.927	27.12	0.938	22.93	0.860	Rain100L Ours-B 0.06×2.7

UHD image restoration. We evaluate ArtIR on UHD-Haze (Wang et al., 2024a) and UHD-Blur (Wang et al., 2024a) for UHD dehazing and deblurring, respectively. The results are reported in Table 8 and Table 9. Although not specifically designed for UHD tasks, our model outperforms the recent ERR (Zhao et al., 2025) algorithm on both benchmarks. In particular, ArtIR achieves PSNR gains of 1.63 dB on UHD-Haze and 0.83 dB on UHD-Blur, while requiring fewer parameters.

Medical image restoration. We evaluate our model on two medical imaging tasks, namely CT image denoising and PET image synthesis, using the AAPM (McCollough et al., 2017) and PolarStar M660 (Yang et al., 2025) datasets, respectively. Following (Yang et al., 2025), we compare against previous methods using PSNR, SSIM, and RMSE. As shown in Tables 10 and 11, our model consistently outperforms the specialized Restore-light (Yang et al., 2025) algorithm on both datasets while requiring fewer parameters, highlighting its potential for medical image restoration.

Remote sensing image restoration. For this task, we train separate models on three subsets of the SateHaze1k dataset (Huang et al., 2020). Results for thin, moderate, and thick haze levels are reported in Table 12. Our method outperforms both task-specific and general image restoration algorithms. In

Table 14: Ablation results. Further ablation studies can be found in the Appendix.

(a) Ablation study for the proposed module.				(0)	rumber c	n segments	III LIXI WI.	(c) Alternative large-kerner operations.				
Method	PSNR	FLOPs	Params	N	PSNR	FLOPs	Params	Method	PSNR	FLOPs	Params	
Conv Block (Base)	31.38	13.32	0.86	2	34.86	12.71	0.83	Depth-wise Conv	36.14	16.81	1.83	
SMA	31.80	12.65	0.81	3	35.75	12.78	0.84	Decomposition	35.70	13.04	0.91	
LKFM w/o channel	36.18	12.81	0.85	4	36.18	12.81	0.85	Frequency-based	35.51	12.92	0.94	
Full	36.92	12.81	0.85	5	36.12	12.83	0.86	Ours	36.92	12.81	0.85	
Tun	30.92	12.01	0.65		30.12	12.65	0.80	Ours	30.92	12.01	0.0	

particular, it surpasses the recent Mamba-based FMambaIR (Luan et al., 2025) across all three subsets in terms of PSNR. These findings indicate the robustness of our model under diverse conditions.

4.5 RUNTIME COMPARISON

We evaluate the runtime efficiency of our model against recent representative algorithms across multiple scenarios. As shown in Table 13, our model is approximately $8 \times$ faster than the Transformer-based MTF-L V2 (Jin et al., 2025) on single-degradation tasks. For the composite degradation task, it achieves a $2.5 \times$ speedup over MoCE-IR-S (Zamfir et al., 2025), which is specifically designed to accelerate inference using Mixtures of Experts. In addition, our model outperforms the all-in-one algorithm, AdaIR (Cui et al., 2025), in runtime efficiency.

4.6 ABLATION STUDIES

For the ablation studies, we train the tiny model on the RESIDE-Indoor dataset (Li et al., 2018) for 100k iterations and evaluate its performance on the SOTS-Indoor dataset (Li et al., 2018). Additional ablation studies on the large-kernel design are included in the Appendix.

Effects of LKFM. In our model, we adopt LKFM in the bottleneck and employ SMA at other scales. As a baseline, we construct a model using convolution blocks in all stages, where the split-and-multiplication operations in SMA are replaced with a 1×1 convolution for channel reduction. This baseline, denoted as Conv Block in Table 14(a), achieves 31.38 dB in PSNR. Our SMA, which incorporates a gated mechanism to regulate information flow, improves performance by 0.42 dB while maintaining higher computational efficiency. Replacing SMA in the bottleneck with our spatial LKFM (without channel attention) yields a 4.38 dB gain with negligible computational overhead. With the addition of lightweight channel attention, the complete model achieves the best performance, surpassing the convolutional baseline by 5.54 dB and further enhancing efficiency.

Multi-scale learning in LKFM. We implement multi-scale representation learning in LKFM by splitting features into segments. To evaluate this design, we conduct ablation experiments with different numbers of segments, as reported in Table 14(b). Overall, performance improves with more segments, confirming the effectiveness of the multi-scale strategy. In the final model, the number of segments is set to 4, providing a better trade-off between accuracy and efficiency.

Alternatives to large-kernel operations. We compare our method with alternative designs by replacing the LKFM in our framework. As shown in Table 14(c), a 63×63 depth-wise convolution achieves 36.14 dB in PSNR. Decomposing this convolution into smaller components following (Wang et al., 2024c), namely, a 13×13 depth-wise convolution, a dilated 9×9 depth-wise convolution with dilation rate 7, and a point-wise convolution, improves efficiency but reduces accuracy. The frequency-based variant (Mao et al., 2023), which applies a 1×1 convolution to the concatenated Fourier real and imaginary components, attains only 35.51 dB in PSNR. In contrast, our method delivers higher accuracy with lower computational cost and fewer parameters.

5 CONCLUSION

This paper presents an efficient and effective network for image restoration by leveraging large-kernel operations. Motivated by the observed channel redundancy in restoration models, we apply adaptive large-kernel operators directly to single-channel feature maps. To recover channel diversity, we introduce a lightweight channel attention mechanism. In addition, to enhance multi-scale learning, we design a fusion module that progressively integrates large-scale contextual information of different sizes with local details. The resulting network attains state-of-the-art performance across three generic image restoration scenarios, namely single-degradation, all-in-one, and composite degradation, while preserving high computational efficiency and fast inference. Furthermore, ArtIR demonstrates strong robustness on domain-specific tasks, including UHD, medical imaging, and remote sensing.

REFERENCES

- Yuang Ai, Huaibo Huang, Xiaoqiang Zhou, Jiexiang Wang, and Ran He. Multimodal prompt perceiver: Empower adaptiveness generalizability and fidelity for all-in-one image restoration. In *CVPR*, 2024.
 - Anas M Ali, Bilel Benjdira, Anis Koubaa, Walid El-Shafai, Zahid Khan, and Wadii Boulila. Vision transformers in image restoration: A survey. *Sensors*, 2023.
- Hanting Chen, Yunhe Wang, Tianyu Guo, Chang Xu, Yiping Deng, Zhenhua Liu, Siwei Ma, Chunjing Xu, Chao Xu, and Wen Gao. Pre-trained image processing transformer. In *CVPR*, 2021a.
 - Honghao Chen, Xiangxiang Chu, Yongjian Ren, Xin Zhao, and Kaiqi Huang. Pelk: Parameter-efficient large kernel convnets with peripheral convolution. In *CVPR*, 2024a.
 - Liangyu Chen, Xiaojie Chu, Xiangyu Zhang, and Jian Sun. Simple baselines for image restoration. In *ECCV*, 2022.
 - Wei-Ting Chen, Hao-Yu Fang, Cheng-Lin Hsieh, Cheng-Che Tsai, I Chen, Jian-Jiun Ding, Sy-Yen Kuo, et al. All snow removed: Single image desnowing algorithm using hierarchical dual-tree complex wavelet representation and contradict channel loss. In *ICCV*, 2021b.
 - Xiang Chen, Hao Li, Mingqiang Li, and Jinshan Pan. Learning a sparse transformer network for effective image deraining. In *CVPR*, 2023.
 - Xiang Chen, Jinshan Pan, and Jiangxin Dong. Bidirectional multi-scale implicit neural representations for image deraining. In *CVPR*, 2024b.
 - Zixuan Chen, Zewei He, and Zhe-Ming Lu. Dea-net: Single image dehazing based on detail-enhanced convolution and content-guided attention. *IEEE TIP*, 2024c.
 - Kaichen Chi, Yuan Yuan, and Qi Wang. Trinity-net: Gradient-guided swin transformer-based remote sensing image dehazing and beyond. *IEEE TGRS*, 2023.
 - Sung-Jin Cho, Seo-Won Ji, Jun-Pyo Hong, Seung-Won Jung, and Sung-Jea Ko. Rethinking coarse-to-fine approach in single image deblurring. In *ICCV*, 2021.
 - Marcos V Conde, Gregor Geigle, and Radu Timofte. High-quality image restoration following human instructions. In *ECCV*, 2024.
 - Yuning Cui, Wenqi Ren, Xiaochun Cao, and Alois Knoll. Focal network for image restoration. In *ICCV*, 2023a.
 - Yuning Cui, Wenqi Ren, Xiaochun Cao, and Alois Knoll. Image restoration via frequency selection. *IEEE TPAMI*, 2023b.
 - Yuning Cui, Wenqi Ren, Sining Yang, Xiaochun Cao, and Alois Knoll. Irnext: Rethinking convolutional network design for image restoration. In *ICML*, 2023c.
 - Yuning Cui, Wenqi Ren, Xiaochun Cao, and Alois Knoll. Revitalizing convolutional network for image restoration. *IEEE TPAMI*, 2024a.
- Yuning Cui, Wenqi Ren, and Alois Knoll. Omni-kernel network for image restoration. In *AAAI*, 2024b.
- Yuning Cui, Syed Waqas Zamir, Salman Khan, Alois Knoll, Mubarak Shah, and Fahad Shahbaz Khan. AdaIR: Adaptive all-in-one image restoration via frequency mining and modulation. In *ICLR*, 2025.
- Xiaohan Ding, Xiangyu Zhang, Jungong Han, and Guiguang Ding. Scaling up your kernels to 31x31:
 Revisiting large kernel design in cnns. In *CVPR*, 2022a.
 - Xiaohan Ding, Xiangyu Zhang, Jungong Han, and Guiguang Ding. Scaling up your kernels to 31x31: Revisiting large kernel design in cnns. In *CVPR*, 2022b.

- Xiaohan Ding, Yiyuan Zhang, Yixiao Ge, Sijie Zhao, Lin Song, Xiangyu Yue, and Ying Shan. Unireplknet: A universal perception large-kernel convnet for audio video point cloud time-series and image recognition. In *CVPR*, 2024.
 - Akshay Dudhane, Omkar Thawakar, Syed Waqas Zamir, Salman Khan, Fahad Shahbaz Khan, and Ming-Hsuan Yang. Dynamic pre-training: Towards efficient and scalable all-in-one image restoration. *arXiv preprint arXiv:2404.02154*, 2024.
 - Qingnan Fan, Dongdong Chen, Lu Yuan, Gang Hua, Nenghai Yu, and Baoquan Chen. A general decoupled learning framework for parameterized image operators. *IEEE TPAMI*, 2019.
 - Daniel Feijoo, Juan C Benito, Alvaro Garcia, and Marcos V Conde. Darkir: Robust low-light image restoration. In *CVPR*, 2025.
 - Ning Gao, Xingyu Jiang, Xiuhui Zhang, and Yue Deng. Efficient frequency-domain image deraining with contrastive regularization. In *ECCV*, 2024.
 - Chun-Le Guo, Qixin Yan, Saeed Anwar, Runmin Cong, Wenqi Ren, and Chongyi Li. Image dehazing transformer with transmission-aware 3d position embedding. In *CVPR*, 2022.
 - Hang Guo, Jinmin Li, Tao Dai, Zhihao Ouyang, Xudong Ren, and Shu-Tao Xia. Mambair: A simple baseline for image restoration with state-space model. In *ECCV*, 2024a.
 - Yu Guo, Yuan Gao, Yuxu Lu, Huilin Zhu, Ryan Wen Liu, and Shengfeng He. Onerestore: A universal restoration framework for composite degradation. In *ECCV*, 2024b.
 - Fangwei Hao, Jiesheng Wu, Ji Du, Yinjie Wang, and Jing Xu. Dilated strip attention network for image restoration. *arXiv preprint arXiv:2407.18613*, 2024.
 - JiaKui Hu, Lujia Jin, Zhengjian Yao, and Yanye Lu. Universal image restoration pre-training via degradation classification. In *ICLR*, 2025a.
 - Quanwei Hu, Yinggan Tang, and Xuguang Zhang. Large kernel modulation network for efficient image super-resolution. *arXiv preprint arXiv:2508.11893*, 2025b.
 - Binghui Huang, Li Zhi, Chao Yang, Fuchun Sun, and Yixu Song. Single satellite optical imagery dehazing using sar image prior based on conditional generative adversarial networks. In *WACV*, 2020.
 - Jia-Bin Huang, Abhishek Singh, and Narendra Ahuja. Single image super-resolution from transformed self-exemplars. In *CVPR*, 2015.
 - Junjun Jiang, Zengyuan Zuo, Gang Wu, Kui Jiang, and Xianming Liu. A survey on all-in-one image restoration: Taxonomy, evaluation and future trends. *IEEE TPAMI*, 2025.
 - Yitong Jiang, Zhaoyang Zhang, Tianfan Xue, and Jinwei Gu. Autodir: Automatic all-in-one image restoration with latent diffusion. In *ECCV*, 2024.
 - Zhi Jin, Yuwei Qiu, Kaihao Zhang, Hongdong Li, and Wenhan Luo. Mb-taylorformer v2: Improved multi-branch linear transformer expanded by taylor formula for image restoration. *arXiv* preprint *arXiv*:2501.04486, 2025.
 - Diederik P Kingma. Adam: A method for stochastic optimization. *arXiv preprint arXiv:1412.6980*, 2014.
- Lingshun Kong, Jiangxin Dong, Jianjun Ge, Mingqiang Li, and Jinshan Pan. Efficient frequency domain-based transformers for high-quality image deblurring. In *CVPR*, 2023.
 - Ashutosh Kulkarni and Subrahmanyam Murala. Aerial image dehazing with attentive deformable transformers. In *WACV*, pp. 6305–6314, 2023.
 - Dongheon Lee, Seokju Yun, and Youngmin Ro. Partial large kernel cnns for efficient super-resolution. *arXiv preprint arXiv:2404.11848*, 2024.

- Dongheon Lee, Seokju Yun, and Youngmin Ro. Emulating self-attention with convolution for efficient image super-resolution. *arXiv preprint arXiv:2503.06671*, 2025.
 - Boyi Li, Wenqi Ren, Dengpan Fu, Dacheng Tao, Dan Feng, Wenjun Zeng, and Zhangyang Wang. Benchmarking single-image dehazing and beyond. *IEEE TIP*, 2018.
 - Boyun Li, Xiao Liu, Peng Hu, Zhongqin Wu, Jiancheng Lv, and Xi Peng. All-in-one image restoration for unknown corruption. In *CVPR*, 2022.
 - Boyun Li, Haiyu Zhao, Wenxin Wang, Peng Hu, Yuanbiao Gou, and Xi Peng. Mair: A locality-and continuity-preserving mamba for image restoration. In *CVPR*, 2025a.
 - Chongyi Li, Chun-Le Guo, man zhou, Zhexin Liang, Shangchen Zhou, Ruicheng Feng, and Chen Change Loy. Embedding fourier for ultra-high-definition low-light image enhancement. In *ICLR*, 2023a.
 - Dachong Li, Li Li, Zhuangzhuang Chen, and Jianqiang Li. Shiftwiseconv: Small convolutional kernel with large kernel effect. In *CVPR*, 2025b.
 - Dong Li, Yidi Liu, Xueyang Fu, Jie Huang, Senyan Xu, Qi Zhu, and Zheng-Jun Zha. Fouriermamba: Fourier learning integration with state space models for image deraining. In *ICML*, 2025c.
 - Yuxuan Li, Qibin Hou, Zhaohui Zheng, Ming-Ming Cheng, Jian Yang, and Xiang Li. Large selective kernel network for remote sensing object detection. In *ICCV*, 2023b.
 - Yuxuan Li, Xiang Li, Yimain Dai, Qibin Hou, Li Liu, Yongxiang Liu, Ming-Ming Cheng, and Jian Yang. Lsknet: A foundation lightweight backbone for remote sensing: Y. li et al. *IJCV*, 2025d.
 - Jingyun Liang, Jiezhang Cao, Guolei Sun, Kai Zhang, Luc Van Gool, and Radu Timofte. Swinir: Image restoration using swin transformer. In *ICCVW*, 2021.
 - Bin Liu, Bing Li, and Shuofeng Li. Lk-unet: Large kernel convolution-driven u-shaped network for semantic segmentation of high-resolution earth surface images. *Advances in Space Research*, 2025.
 - Shiwei Liu, Tianlong Chen, Xiaohan Chen, Xuxi Chen, Qiao Xiao, Boqian Wu, Tommi Kärkkainen, Mykola Pechenizkiy, Decebal C Mocanu, and Zhangyang Wang. More convnets in the 2020s: Scaling up kernels beyond 51x51 using sparsity. In *ICLR*, 2023.
 - Ye Liu, Lei Zhu, Shunda Pei, Huazhu Fu, Jing Qin, Qing Zhang, Liang Wan, and Wei Feng. From synthetic to real: Image dehazing collaborating with unlabeled real data. In *ACM MM*, 2021.
 - Yun-Fu Liu, Da-Wei Jaw, Shih-Chia Huang, and Jenq-Neng Hwang. Desnownet: Context-aware deep network for snow removal. *IEEE TIP*, 2018.
 - Zhuang Liu, Hanzi Mao, Chao-Yuan Wu, Christoph Feichtenhofer, Trevor Darrell, and Saining Xie. A convnet for the 2020s. In *CVPR*, 2022.
 - Xin Luan, Huijie Fan, Qiang Wang, Nan Yang, Shiben Liu, Xiaofeng Li, and Yandong Tang. Fmambair: A hybrid state space model and frequency domain for image restoration. *TGRS*, 2025.
 - Pinjun Luo, Guoqiang Xiao, Xinbo Gao, and Song Wu. Lkd-net: Large kernel convolution network for single image dehazing. In *ICME*, 2023.
 - Yanmei Luo, Luping Zhou, Bo Zhan, Yuchen Fei, Jiliu Zhou, Yan Wang, and Dinggang Shen. Adaptive rectification based adversarial network with spectrum constraint for high-quality pet image synthesis. *Medical Image Analysis*, 2022.
 - Ziwei Luo, Fredrik K Gustafsson, Zheng Zhao, Jens Sjölund, and Thomas B Schön. Controlling vision-language models for universal image restoration. In *ICLR*, 2024.
 - Achleshwar Luthra, Harsh Sulakhe, Tanish Mittal, Abhishek Iyer, and Santosh Yadav. Eformer: Edge enhancement based transformer for medical image denoising. *arXiv preprint arXiv:2109.08044*, 2021.

- Xu Ma, Xiyang Dai, Yue Bai, Yizhou Wang, and Yun Fu. Rewrite the stars. In *CVPR*, 2024a.
- Xu Ma, Xiyang Dai, Jianwei Yang, Bin Xiao, Yinpeng Chen, Yun Fu, and Lu Yuan. Efficient
 modulation for vision networks. In *ICLR*, 2024b.
 - Xintian Mao, Yiming Liu, Fengze Liu, Qingli Li, Wei Shen, and Yan Wang. Intriguing findings of frequency selection for image deblurring. In *AAAI*, 2023.
 - David Martin, Charless Fowlkes, Doron Tal, and Jitendra Malik. A database of human segmented natural images and its application to evaluating segmentation algorithms and measuring ecological statistics. In *ICCV*, 2001.
 - Cynthia H McCollough, Adam C Bartley, Rickey E Carter, Baiyu Chen, Tammy A Drees, Phillip Edwards, David R Holmes III, Alice E Huang, Farhana Khan, Shuai Leng, et al. Low-dose ct for the detection and classification of metastatic liver lesions: results of the 2016 low dose ct grand challenge. *Medical physics*, 2017.
 - Şaban Öztürk, Oğuz Can Duran, and Tolga Çukur. Denomamba: A fused state-space model for low-dose ct denoising. *arXiv preprint arXiv:2409.13094*, 2024.
 - Namuk Park and Songkuk Kim. How do vision transformers work? In ICLR, 2022.
 - Vaishnav Potlapalli, Syed Waqas Zamir, Salman H Khan, and Fahad Shahbaz Khan. Promptir: Prompting for all-in-one image restoration. In *NeurIPS*, 2023.
 - Yuwei Qiu, Kaihao Zhang, Chenxi Wang, Wenhan Luo, Hongdong Li, and Zhi Jin. Mb-taylorformer: Multi-branch efficient transformer expanded by taylor formula for image dehazing. In *ICCV*, 2023.
 - Sudarshan Rajagopalan, Nithin Gopalakrishnan Nair, Jay N Paranjape, and Vishal M Patel. Gendeg: Diffusion-based degradation synthesis for generalizable all-in-one image restoration. In *CVPR*, 2025.
 - Wenqi Ren, Si Liu, Hua Zhang, Jinshan Pan, Xiaochun Cao, and Ming-Hsuan Yang. Single image dehazing via multi-scale convolutional neural networks. In *ECCV*, 2016.
 - Wenqi Ren, Jinshan Pan, Hua Zhang, Xiaochun Cao, and Ming-Hsuan Yang. Single image dehazing via multi-scale convolutional neural networks with holistic edges. *IJCV*, 2020.
 - Franzen Rich. Kodak lossless true color image suite. http://r0k.us/graphics/kodak, 1999.
 - Lingyan Ruan, Mojtaba Bemana, Hans-peter Seidel, Karol Myszkowski, and Bin Chen. Revisiting image deblurring with an efficient convnet. *arXiv preprint arXiv:2302.02234*, 2023.
 - Qijun Shi, Hongjian Zhan, Yangfu Li, Weijun Zou, Huasheng Li, Umapada Pal, and Yue Lu. Lk-net: Efficient large kernel convnet for document enhancement. In *ICPR*, 2024.
 - Hyeongseok Son, Junyong Lee, Sunghyun Cho, and Seungyong Lee. Single image defocus deblurring using kernel-sharing parallel atrous convolutions. In *ICCV*, 2021.
 - Yuda Song, Zhuqing He, Hui Qian, and Xin Du. Vision transformers for single image dehazing. *IEEE TIP*, 2023.
 - Xiangpeng Tian, Xiangyu Liao, Xiao Liu, Meng Li, and Chao Ren. Degradation-aware feature perturbation for all-in-one image restoration. In *CVPR*, 2025.
 - Fu-Jen Tsai, Yan-Tsung Peng, Yen-Yu Lin, Chung-Chi Tsai, and Chia-Wen Lin. Stripformer: Strip transformer for fast image deblurring. In *ECCV*, 2022.
 - Jeya Maria Jose Valanarasu, Rajeev Yasarla, and Vishal M. Patel. Transweather: Transformer-based restoration of images degraded by adverse weather conditions. In *CVPR*, 2022.
 - Ashish Vaswani, Noam Shazeer, Niki Parmar, Jakob Uszkoreit, Llion Jones, and Aidan N Gomez. Attention is all you need. *NeurIPS*, 2017.

- Cong Wang, Jinshan Pan, Wei Wang, Gang Fu, Siyuan Liang, Mengzhu Wang, Xiao-Ming Wu, and Jun Liu. Correlation matching transformation transformers for uhd image restoration. In *AAAI*, 2024a.
 - Dayang Wang, Fenglei Fan, Zhan Wu, Rui Liu, Fei Wang, and Hengyong Yu. Ctformer: convolution-free token2token dilated vision transformer for low-dose ct denoising. *Physics in Medicine & Biology*, 2023.
 - Liyan Wang, Cong Wang, Jinshan Pan, Weixiang Zhou, Xiaoran Sun, Wei Wang, and Zhixun Su. Ultra-high-definition restoration: New benchmarks and a dual interaction prior-driven solution. *arXiv e-prints*, 2024b.
 - Tianyu Wang, Xin Yang, Ke Xu, Shaozhe Chen, Qiang Zhang, and Rynson W.H. Lau. Spatial attentive single-image deraining with a high quality real rain dataset. In *CVPR*, 2019.
 - Yan Wang, Yusen Li, Gang Wang, and Xiaoguang Liu. Multi-scale attention network for single image super-resolution. In *CVPR*, 2024c.
 - Yuhao Wang and Wei Xi. Uniconvnet: Expanding effective receptive field while maintaining asymptotically gaussian distribution for convnets of any scale. In *ICCV*, 2025.
 - Zhendong Wang, Xiaodong Cun, Jianmin Bao, Wengang Zhou, Jianzhuang Liu, and Houqiang Li. Uformer: A general u-shaped transformer for image restoration. In *CVPR*, 2022.
 - Yuanbo Wen, Tao Gao, Jing Zhang, Ziqi Li, and Ting Chen. Encoder-free multiaxis physics-aware fusion network for remote sensing image dehazing. *TGRS*, 2023.
 - Jiangwei Weng, Zhiqiang Yan, Ying Tai, Jianjun Qian, Jian Yang, and Jun Li. Mamballie: Implicit retinex-aware low light enhancement with global-then-local state space. In *NeurIPS*, 2024.
 - Sanghyun Woo, Jongchan Park, Joon-Young Lee, and In So Kweon. Cbam: Convolutional block attention module. In *ECCV*, 2018.
 - Gang Wu, Junjun Jiang, Kui Jiang, and Xianming Liu. Harmony in diversity: Improving all-in-one image restoration via multi-task collaboration. In *ACM MM*, 2024.
 - Chengxing Xie, Xiaoming Zhang, Linze Li, Haiteng Meng, Tianlin Zhang, Tianrui Li, and Xiaole Zhao. Large kernel distillation network for efficient single image super-resolution. In *CVPR*, 2023.
 - Ruihan Xu, Haokui Zhang, Wenze Hu, Shiliang Zhang, and Xiaoyu Wang. Parcnetv2: Oversized kernel with enhanced attention. In *CVPR*, 2023.
 - Wenhan Yang, Robby T. Tan, Jiashi Feng, Jiaying Liu, Zongming Guo, and Shuicheng Yan. Deep joint rain detection and removal from a single image. In *CVPR*, 2017.
 - Zhiwen Yang, Yang Zhou, Hui Zhang, Bingzheng Wei, Yubo Fan, and Yan Xu. Drmc: a generalist model with dynamic routing for multi-center pet image synthesis. In *MICCAI*, 2023.
 - Zhiwen Yang, Jiayin Li, Hui Zhang, Dan Zhao, Bingzheng Wei, and Yan Xu. Restore-rwkv: Efficient and effective medical image restoration with rwkv. *arXiv preprint arXiv:2407.11087*, 2025.
 - Shunsuke Yasuki and Masato Taki. Cam back again: Large kernel cnns from a weakly supervised object localization perspective. In *CVPR*, 2024.
 - Tian Ye, Yunchen Zhang, Mingchao Jiang, Liang Chen, Yun Liu, Sixiang Chen, and Erkang Chen. Perceiving and modeling density for image dehazing. In *ECCV*, 2022.
 - Weihao Yu, Mi Luo, Pan Zhou, Chenyang Si, Yichen Zhou, Xinchao Wang, Jiashi Feng, and Shuicheng Yan. Metaformer is actually what you need for vision. In *CVPR*, 2022.
- Eduard Zamfir, Zongwei Wu, Nancy Mehta, Yuedong Tan, Danda Pani Paudel, Yulun Zhang, and Radu Timofte. Complexity experts are task-discriminative learners for any image restoration. In *CVPR*, 2025.

- Syed Waqas Zamir, Aditya Arora, Salman Khan, Munawar Hayat, Fahad Shahbaz Khan, and Ming-Hsuan Yang. Restormer: Efficient transformer for high-resolution image restoration. In CVPR, 2022.
 - He Zhang and Vishal M Patel. Density-aware single image de-raining using a multi-stream dense network. In *CVPR*, 2018.
 - Jinghao Zhang, Jie Huang, Mingde Yao, Zizheng Yang, Hu Yu, Man Zhou, and Feng Zhao. Ingredient-oriented multi-degradation learning for image restoration. In *CVPR*, 2023.
 - Richard Zhang, Phillip Isola, Alexei A Efros, Eli Shechtman, and Oliver Wang. The unreasonable effectiveness of deep features as a perceptual metric. In *CVPR*, 2018a.
 - Xu Zhang, Jiaqi Ma, Guoli Wang, Qian Zhang, Huan Zhang, and Lefei Zhang. Perceive-ir: Learning to perceive degradation better for all-in-one image restoration. *IEEE TIP*, 2025a.
 - Yulun Zhang, Kunpeng Li, Kai Li, Lichen Wang, Bineng Zhong, and Yun Fu. Image super-resolution using very deep residual channel attention networks. In *ECCV*, 2018b.
 - Zhicheng Zhang, Lequan Yu, Xiaokun Liang, Wei Zhao, and Lei Xing. Transct: dual-path transformer for low dose computed tomography. In *MICCAI*, 2021.
 - Zilong Zhang, Chujie Qin, Chunle Guo, Yong Zhang, Chao Xue, Ming-Ming Cheng, and Chongyi Li. Ram++: Robust representation learning via adaptive mask for all-in-one image restoration. *arXiv* preprint arXiv:2509.12039, 2025b.
 - Chen Zhao, Zhizhou Chen, Yunzhe Xu, Enxuan Gu, Jian Li, Zili Yi, Qian Wang, Jian Yang, and Ying Tai. From zero to detail: Deconstructing ultra-high-definition image restoration from progressive spectral perspective. In *CVPR*, 2025.
 - Zhuoran Zheng, Wenqi Ren, Xiaochun Cao, Xiaobin Hu, Tao Wang, Fenglong Song, and Xiuyi Jia. Ultra-high-definition image dehazing via multi-guided bilateral learning. In *CVPR*, 2021.
 - Long Zhou, Joshua D Schaefferkoetter, Ivan WK Tham, Gang Huang, and Jianhua Yan. Supervised learning with cyclegan for low-dose fdg pet image denoising. *Medical image analysis*, 2020.
 - Man Zhou, Jie Huang, Chun-Le Guo, and Chongyi Li. Fourmer: An efficient global modeling paradigm for image restoration. In *ICML*, 2023.
 - Shangchen Zhou, Chongyi Li, and Chen Change Loy. Lednet: Joint low-light enhancement and deblurring in the dark. In *ECCV*, 2022a.
 - Yang Zhou, Zhiwen Yang, Hui Zhang, Eric I-Chao Chang, Yubo Fan, and Yan Xu. 3d segmentation guided style-based generative adversarial networks for pet synthesis. *IEEE TMI*, 2022b.
 - Yurui Zhu, Tianyu Wang, Xueyang Fu, Xuanyu Yang, Xin Guo, Jifeng Dai, Yu Qiao, and Xiaowei Hu. Learning weather-general and weather-specific features for image restoration under multiple adverse weather conditions. In *CVPR*, 2023.
 - Zhen Zou, Hu Yu, Jie Huang, and Feng Zhao. Freqmamba: Viewing mamba from a frequency perspective for image deraining. In *ACM MM*, 2024.

A APPENDIX

A.1 IMPLEMENTATION DETAILS

This section outlines the implementation details for various image restoration settings. To ensure fair comparison, we scale our model by adjusting the number of blocks and channels at each scale of the encoder and decoder. The specifications of the three model variants are summarized in Table 15. In practice, the *expand* operation in LKFM is implemented by interleaving features along the channel dimension, duplicating each channel to achieve expansion. FLOPs are measured on $256 \times 256 \times 3$ patches, and all experiments are conducted on NVIDIA Tesla A100 GPUs. The model used in the experiments of Figure 4 corresponds to Table 14(b) with N=2. Following (Cui et al., 2024b), the kernel size is increased to 63.

For fairness, no additional training tricks are applied. The code and pre-trained models will be released publicly. The ChatGPT 5 model is used to polish writing.

Table 15: Architectural specifications of the three variants of the proposed network.

Variant	$[L_1, L_2, L_3, L_4]$	Num. of Channels	Params	FLOPs
Ours-T (Tiny) Ours-S (Small) Ours-B (Base)	[1, 1, 1, 4]	[32, 64, 128, 128, 64, 32, 32]	0.85M	12.76G
	[2, 3, 4, 4]	[32, 64, 128, 128, 64, 32, 32]	2.46M	23.73G
	[3, 3, 6, 4]	[48, 96, 192, 192, 96, 48, 48]	7.27M	63.14G

The runtime evaluation is performed on an NVIDIA RTX 4090 GPU. Scores are reported as the average runtime over all images in the corresponding datasets. For the mixed-degradation task, we use the low-light image enhancement dataset, while for the all-in-one task, we adopt Rain100L (Yang et al., 2017).

Single-degradation image restoration. The model is trained separately on each dataset using the Adam optimizer (Kingma, 2014) with an initial learning rate of 1×10^{-3} , which is gradually reduced to 1×10^{-7} via cosine annealing. Training follows prior arts (Cui et al., 2023a; Cho et al., 2021), using the dual-domain L_1 loss and typically running for 300k iterations (Zamir et al., 2022). For deraining datasets, consistent with previous methods (Zamir et al., 2022; Chen et al., 2023), evaluation is performed on the Y channel of the YCbCr color space.

All-in-one image restoration. Our dataset preparation follows previous works (Potlapalli et al., 2023; Cui et al., 2025), as summarized in Table 16. The model is trained on a compound dataset collected from five tasks: dehazing, deraining, denoising, deblurring, and low-light image enhancement. For denoising, noisy images are generated by adding Gaussian noise with levels $\sigma \in \{15, 25, 50\}$ to clean images. Training configurations largely follow prior methods (Potlapalli et al., 2023; Cui et al., 2025). Specifically, the model is trained on $128 \times 128 \times 3$ patches for 130 epochs with a batch size of 32 and an initial learning rate of 2×10^{-4} .

Table 16: Summary of datasets used in all-in-one experiments.

Setting	Dehazing	Deraining	Denoising	Deblurring	Enhancement
Train	RESIDE	Rain100L	WED, BSD400	GOPRO	LOL
Test	SOTS	Rain100L	BSD68, Urban100, Kodak24	GOPRO	LOL

Composite degradation image restoration. The basic setup for this task follows that of the single-degradation setting.

Domain-specific image restoration tasks. The training and dataset configurations for UHD, medical imaging, and remote sensing follow representative methods in each domain (Yang et al., 2025; Zhao et al., 2025; Luan et al., 2025), without introducing additional strategies to enhance performance.

A.2 MORE RELATED WORK: MULTI-TASK IMAGE RESTORATION

Recently, multi-task image restoration has attracted considerable attention for its ability to address multiple degradations within a single model (Fan et al., 2019; Zhu et al., 2023; Jiang et al., 2025; 2024; Zhang et al., 2025b; Ai et al., 2024; Tian et al., 2025; Rajagopalan et al., 2025; Hu et al., 2025a). In this study, we evaluate ArtIR under two multi-task settings: all-in-one and composite degradation. Existing all-in-one methods commonly follow a two-step paradigm: first extracting degradation information from inputs, and then using this information for degradation-aware restoration. For example, AirNet (Li et al., 2022) contrastively extracts degradation cues from degraded images, while PromptIR (Potlapalli et al., 2023) embeds informative features into learnable parameters. More recently, large models and additional modalities have been introduced to derive more discriminative features from inputs (Zhang et al., 2025a; Conde et al., 2024; Luo et al., 2024). Another line of work explores dynamic learning mechanisms (e.g., Mixtures of Experts) to coordinate different sub-tasks and improve efficiency (Wu et al., 2024; Zamfir et al., 2025; Dudhane et al., 2024). For composite degradations, OneRestore (Guo et al., 2024b) develops a scene descriptor-guided Transformer that incorporates both visual and textual inputs (Zhou et al., 2022a; Feijoo et al., 2025).

In contrast to these approaches, we investigate the use of large-kernel operations for multi-task image restoration. Despite not relying on explicit degradation priors, our model achieves performance competitive with state-of-the-art algorithms while maintaining high efficiency. This advantage primarily arises from its strong representational capacity and adaptive learning mechanism. We hope that our model can serve as a solid baseline for future research in this area.

A.3 EVALUATION USING PERCEPTUAL METRICS

In addition to distortion-based metrics, we evaluate our pre-trained all-in-one model using the perceptual metric LPIPS (Zhang et al., 2018a) and compare it with the state-of-the-art all-in-one algorithm (Cui et al., 2025). As shown in Table 17, our model achieves lower LPIPS scores than the competing method across most noise levels.

Table 17: LPIPS (↓, lower is better) comparison with the state-of-the-art all-in-one method (Cui et al., 2025) on three denoising datasets.

	BSD68			Urban100			Kodak24		
Method	$\sigma = 15$	$\sigma = 25$	$\sigma = 50$	$\sigma = 15$	$\sigma = 25$	$\sigma = 50$	$\sigma = 15$	$\sigma = 25$	$\sigma = 50$
AdaIR	0.0634	0.1114	0.2105	0.0419	0.0660	0.1221	0.0835	0.1299	0.2259
Ours-B	0.0599	0.1099	0.2157	0.0388	0.0645	0.1213	0.0790	0.1273	0.2259

A.4 MORE ABLATION STUDIES

Channel attention. We propose an extremely lightweight channel attention mechanism within our LKM. For comparison, we evaluate a full-size channel attention variant that generates attention weights directly from the original input features (e.g., X in Figure 3(d)). This variant attains 36.9 dB in PSNR, which is slightly lower (-0.2 dB) than our design, while introducing an additional 0.05M parameters. These results demonstrate the effectiveness and efficiency of our approach.

Convolution or copy? In our LKFM, we align the channel dimensions of different segments by simply duplicating features, motivated by the channel redundancy observed in image restoration models. To assess this choice, we replace the duplication with convolutional layers for channel adjustment, which yields 36.19 dB in PSNR, 0.1 dB higher than our design, but at the cost of increased FLOPs (+0.09G) and parameters (+0.02M). Considering the trade-off, we adopt channel replication for its simplicity and efficiency.

Alternatives to obtaining the single-channel feature. We explore different lightweight strategies for generating the single-channel feature in LKM. As shown in Table 18, max pooling yields 35.81 dB in PSNR. Concatenating max-pooled and average-pooled features (Woo et al., 2018) followed by a 7×7 convolution for channel reduction slightly improves performance to 35.88 dB. Directly selecting a single input channel (the last channel) achieves the same performance as max pooling. In

contrast, average pooling produces the best results, and we therefore adopt this strategy in our final model.

Table 18: Alternative strategies for obtaining the single-channel feature map.

Method	Max pooling	Max+Avg pooling	Last channel	Ours
PSNR	35.81	35.88	35.81	36.18

Adaptive strategy. We adopt a learnable convolutional layer in our LKM to enable adaptive processing of different inputs. To assess its effectiveness, we replace this dynamic operator with a simplified variant that applies a 63×63 depth-wise convolution to the single-channel feature to generate attention weights, which are then applied via multiplication. This alternative attains only 32.3 dB in PSNR, 3.88 dB lower than our design, despite slightly reduced computational overhead and parameters (-0.13 GLOPs, -0.03M parameters).

A.5 DISCUSSION

The design of our large-kernel operation is inspired by the channel redundancy observed in image restoration models. To further illustrate this phenomenon, we visualize channel similarity results for additional models, including both Transformer- and convolution-based architectures. As shown in Figure 6, different channels often exhibit strong similarities and may learn overlapping representations, albeit to varying degrees. In our model, we adopt an extreme strategy by applying the large-kernel operation to a single-channel feature. A promising direction for future work is to explore which channels, and how many, should share large-kernel operations. However, under the current design, such an extension would inevitably increase computational overhead.

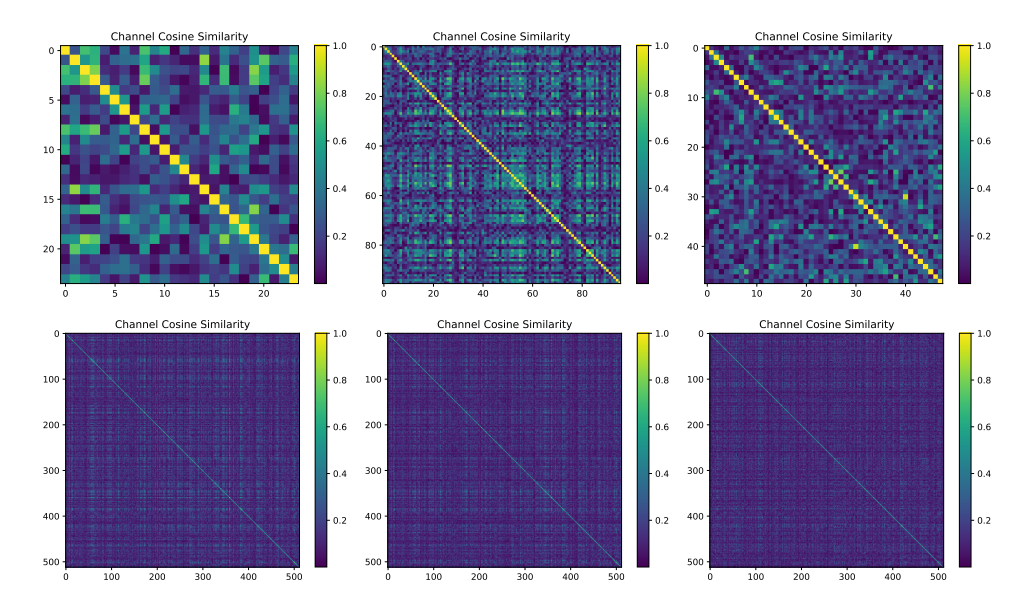


Figure 6: Visualizations of channel similarity for additional models: the Transformer-based MTF-L V2 (Jin et al., 2025) (top) and the convolutional NAFNet baseline (Chen et al., 2022) (bottom).

A.6 MORE VISUAL RESULTS

We first present the t-SNE results of representations learned by our all-in-one model. As shown in Figure 7, the model learns discriminative features for different inputs without relying on explicit priors, highlighting the strong representational capacity of our design.

Furthermore, we visualize the feature maps learned by the local segment and the first large-kernel operator in our LKFM. As shown in Figure 8, the local channel segment captures detailed features,

while the large-kernel operation provides broader contextual perception, demonstrating the effectiveness of our design. The two groups of visualized features are extracted from different LKB in the bottleneck of the all-in-one model.

Finally, we provide additional visual comparisons across various image restoration settings, including single-degradation (Figure 9), all-in-one (Figures 10, 11, 12), and composite degradation (Figure 13).

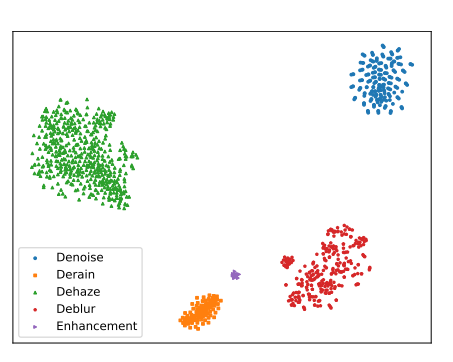


Figure 7: t-SNE visualization of the learned feature representations in our all-in-one model.

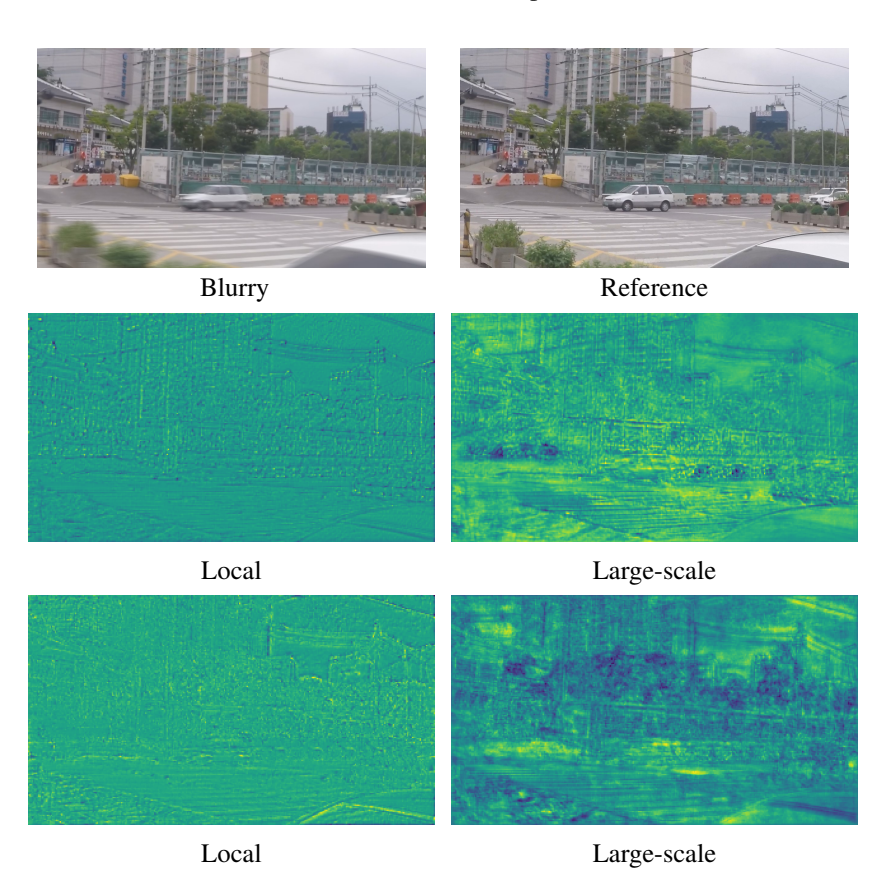


Figure 8: Visualizations of feature maps learned in our LKFM.

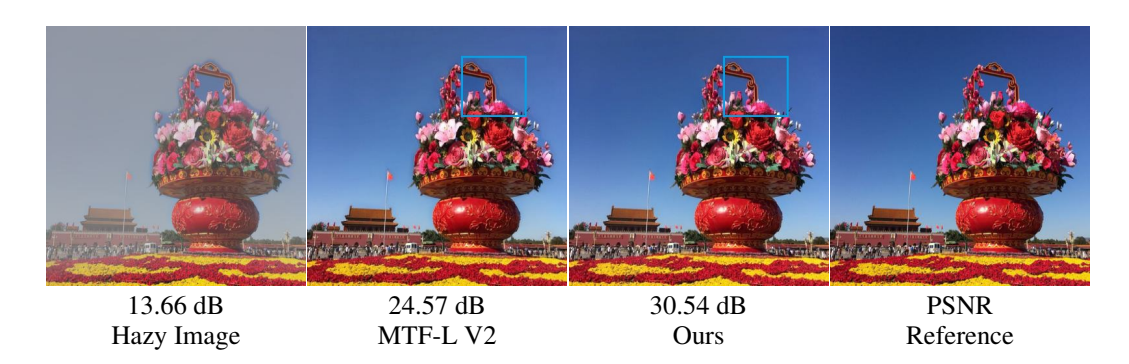


Figure 9: Dehazing results on Haze4K (Liu et al., 2021) under the single-degradation setting.

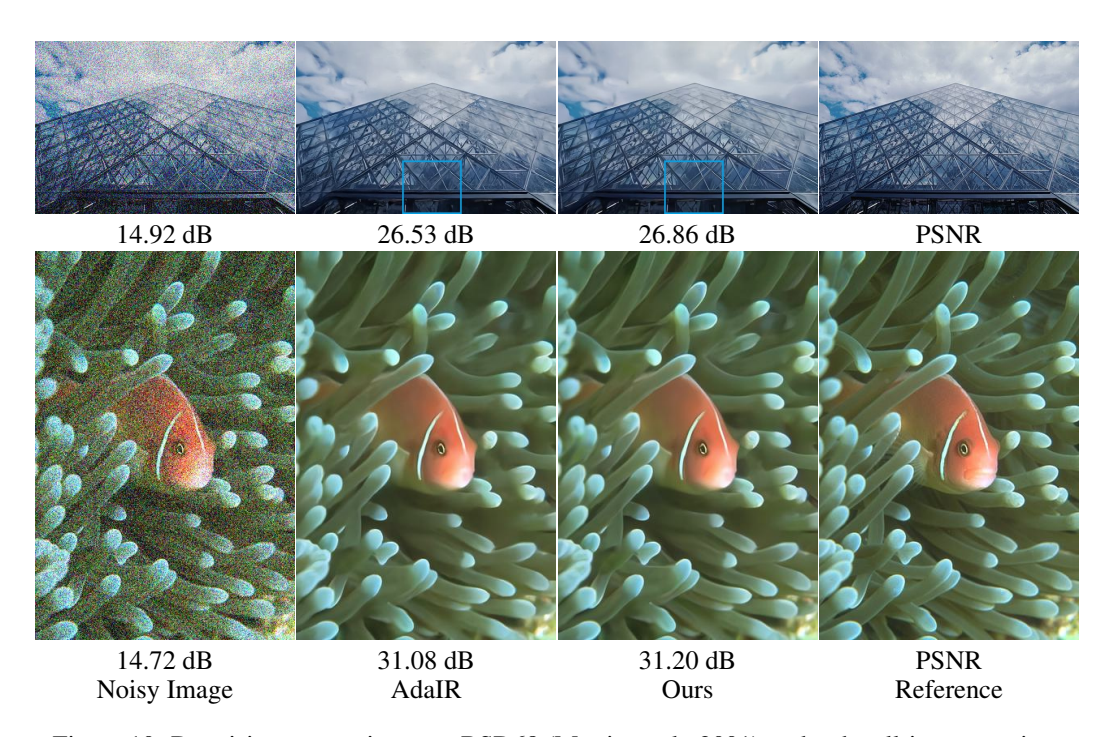


Figure 10: Denoising comparisons on BSD68 (Martin et al., 2001) under the all-in-one setting.

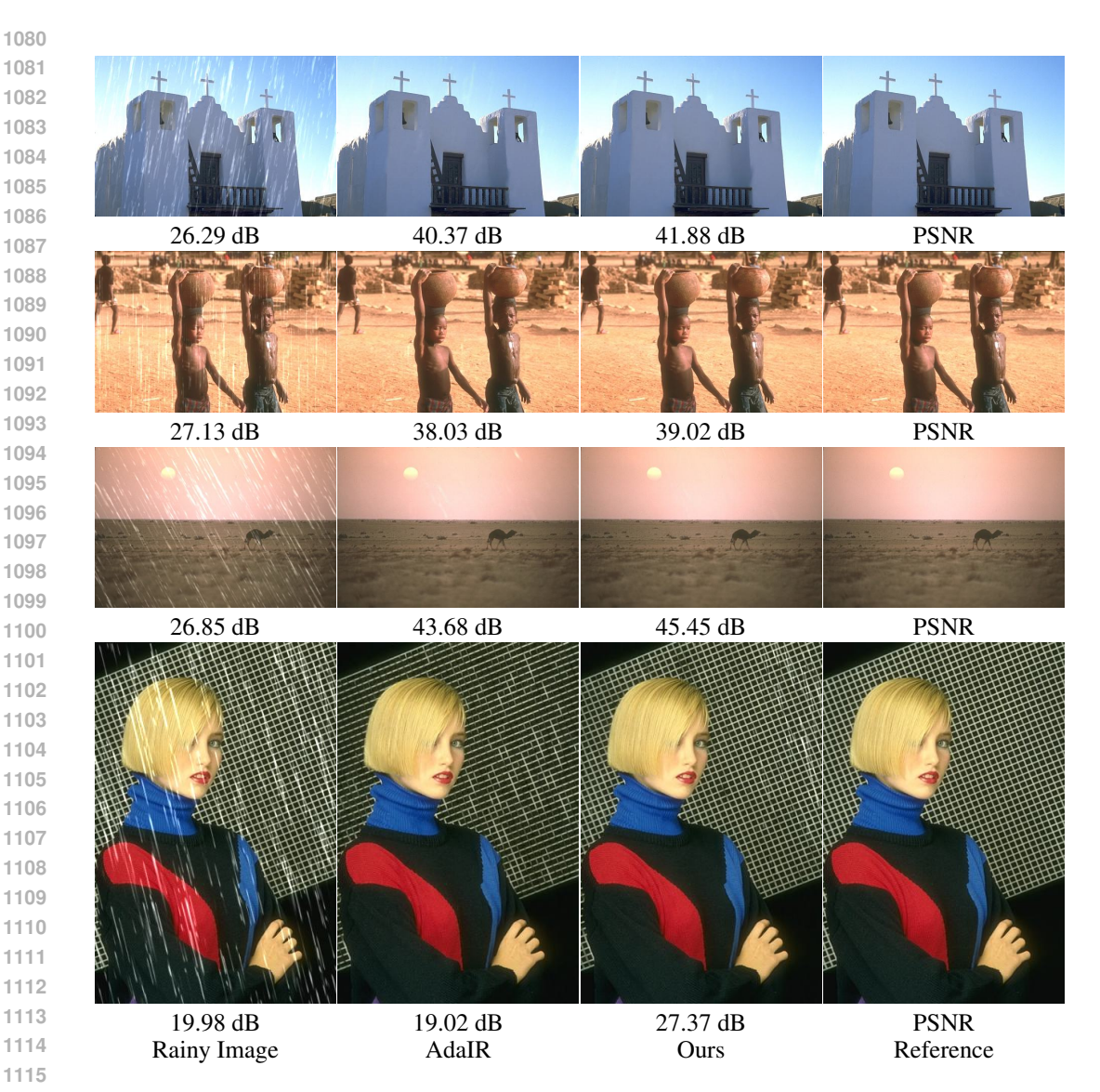


Figure 11: Deraining comparisons on Rain100L (Yang et al., 2017) under the all-in-one setting.



Figure 12: Dehazing comparisons on SOTS-Outdoor (Li et al., 2018) under the all-in-one setting.



Figure 13: Visual results on CDD-11 (Guo et al., 2024b) for composite degradation image restoration.